The Strength of the Spatially Interconnected Eutectic Network in HPDC Mg-La, Mg-Nd, and Mg-La-Nd Alloys

BAO ZHANG, SERGE GAVRAS, ANUMALASETTY V. NAGASEKHAR, CARLOS HORACIO CÁCERES, and MARK A. EASTON

3D numerical images of the intergranular percolating eutectic of two binary alloys, Mg-0.62 at. pctLa and Mg-0.60 at. pctNd, created using dual beam FIB tomography, were incorporated into an FEM code to model their tensile behavior. Due to its high volume fraction (29.9 pct), the behavior of the Mg-La network was akin to that of a stretch-dominated micro-truss structure, whereas the Mg-Nd's, with a relatively low volume fraction (7.5 pct), mimicked that of a bending-dominated structure. The 3D network contributed some 37 MPa to the strength of the Mg-La alloy casting, whereas it only added about 1.4 MPa to the Mg-Nd's. The model predictions based on the binary alloys were verified using cast-to-shape specimens of the Mg-La and two ternary Mg-La-Nd alloys, subjected to a flash-annealing aiming at breaking up the continuity of the 3D network, while preserving the rest of the microstructure unchanged. The flash-annealed specimens exhibited a decrease in strength that matched closely the computed values. Implications regarding alloy design involving the eutectic network and solid solution hardening of more complex alloys are discussed.

DOI: 10.1007/s11661-014-2416-9

I. INTRODUCTION

THE volume fraction of eutectic in high pressure die cast (HPDC) Mg alloys may be as high as 30 pct, and a number of workers[1–7] have suggested that because of the profuse spatial interconnection it should account for a measurable fraction of the casting's strength in excess of the contribution stemming from dispersion hardening. Recent focused ion beam (FIB) sectioning and reconstruction work on cast-to-shape tensile specimens[3,8] of HPDC AZ91D alloy showed that the spatial interconnection of the percolating β-$Mg_{17}Al_{12}$ eutectic involved as much as 95 pct of the intermetallic near the casting surface, or skin region, dropping to about 50 pct at the center of the cross section, or casting core. Numerical modeling of the deformation behavior of the eutectic network showed that it adds ~7 MPa to the specimens' strength,[9] or about 5 pct of its total strength exclusively through the spatial interconnection. Similar modeling for a Mg-Ce alloy showed that the strengthening stemming from the 3D network may be as high as 25 MPa, or about 17 pct of the total strength.[10]

The present study extends the authors' prior modelling work on AZ91 and Mg-Ce alloys[9,10] to two binary Mg-RE alloys, Mg-0.62 at. pctLa, and a Mg-0.60 at. pctNd. FIB tomography was used to determine the 3D morphological features of the percolating networks, and finite element modelling (FEM) *via* ABAQUS codes was used to characterize their deformation behavior and estimate their concomitant strengthening effects. The results of the modelling were subsequently validated using two ternary Mg-La-Nd alloys of a parallel study.[11]

The two binary alloys used for the FEM modelling were from the same batches studied in Reference 7. The two alloys were deliberately chosen with the same at. pct content of solute, but widely different solute solubility and eutectic composition, *i.e.*, widely different amounts of eutectic present in the cast microstructure. Because of the low solubility of La, the Mg-La alloy was expected to gain little strength from solid solution, however, the volume fraction of eutectic should be quite high (~30 pct) and was likely to have a substantive contribution to strength. It was, therefore, expected to be a good model alloy to assess the reinforcing effect of a high volume fraction of intergranular 3D network embedded in a matrix of nearly pure Mg. The Mg-Nd alloy, in comparison, was meant to represent an alloy with large solid solution strengthening and limited contribution from the 3D network because of its relatively low content of eutectic intermetallic (Mg_3Nd is formed

BAO ZHANG, Research Associate, formerly with ARC Centre of Excellence for Design in Light Metals, Materials Engineering, School of Engineering, The University of Queensland, Brisbane, QLD 4072, Australia, is now with Imperial College, London, U.K. SERGE GAVRAS, Postgraduate Student, is with the CAST Co-operative Research Centre, Department of Materials Engineering, Monash University, Monash, VIC 3800, Australia. ANUMALASETTY V. NAGASEKHAR, Research Metallurgist, formerly with ARC Centre of Excellence for Design in Light Metals, Materials Engineering, School of Engineering, The University of Queensland, is now with Carpenter Technology Corporation, PO Box 14662, Reading, PA. CARLOS HORACIO CÁCERES, Reader, is with ARC Centre of Excellence for Design in Light Metals, Materials Engineering, School of Engineering, The University of Queensland. Contact e-mail: c.caceres@uq.edu.au MARK A. EASTON, Professor, formerly with CAST Co-operative Research Centre, Department of Materials Engineering, Monash University, also with Royal Melbourne Institute of Technology, Melbourne, VIC, Australia, is now with School of Aerospace, Mechanical and Manufacturing Engineering, RMIT University, Carlton, VIC 3053, Australia.

Manuscript submitted November 27, 2013.
Article published online June 21, 2014

rather than $Mg_{12}Nd$ in the as-cast state[12]). In this way, the two binary alloys were meant to represent upper and lower bounds to the reinforcing effects of the percolating eutectic network, all other microstructural elements remaining either constant (grain size), or well accounted for (solid solution hardening). The two ternary alloys used to validate the model were selected to represent the microstructures (*i.e.*, the amount of both eutectic and solute in solution) of the binary model alloys, as well as that of current commercial creep resistant Mg alloys containing multiple rare earths (RE's).[7]

The model's validation was done by comparing the strength of the as-cast specimens with specimens subject to short heat-treatments (hereafter referred to as flash-anneals), meant to break up the spatial interconnection of the intermetallic, while preserving the rest of the microstructure unchanged. The flash-anneals were applied to one of the binaries (Mg-La) and the two ternary Mg-La-Nd alloys.[11]

At first sight the approach followed in the present work, *i.e.*, modelling two binary alloys to predict the behavior of two ternary alloys, in turn meant to represent more complex commercial alloys may appear unnecessarily convoluted. The rationale for the approach stems from current industrial practice[7,11,12]: RE are often added to Mg alloys as mischmetal, which in itself is a naturally occuring mixture of Ce, La, Nd, and other RE metals in small proportion. That is, unlike other alloy systems where each of the components is added separately to fulfill a specific purpose, the RE's are added in combination, and therefore, the effects are also a combination apportioned by the individual contents and solubilities. That is, using binary alloys for the first stage of the modeling, more than just a first step in a systematic approach, is a true deconvolution procedure imposed by the way the RE's are available.

II. MATERIALS AND DATA FOR ANALYSIS

A. *Alloys*

The composition of the alloys studied is listed in Table I.

Table I. Chemical Compositions (Atomic Percent) of the Alloys as Determined by ICP-AES

Binary alloys	Mg-0.62 La
(same as those of Ref. [7])	Mg-0.60 Nd
Ternary alloys	Mg-0.47 La-0.10 Nd
(same as those of Ref. [11])	Mg-0.45 La-0.63 Nd

B. *3D Microstructures*

Dual beam FIB tomography was used to characterize the 3D microstructural features of cast-to-shape tensile specimens of the binary alloys of Table I. For both alloys, a volume adjacent to a corner of the specimen's cross section, representing the finest microstructure of the casting's skin, was serially sectioned into 0.2-μm-thick slices on a FIB machine and SEM secondary electron images collected after each slice was removed. The images were subsequently aligned, followed by sequential segmentation and reconstruction to obtain the 3D microstructure of the eutectic. Table II lists the relevant parameters.

C. *Flash-Anneals, Tensile Testing*

Specimens of the ternary alloys and the binary Mg-0.62 at. pctLa were given a flash-anneal, consisting of 1 hour at 793 K (520 °C) followed by water quench, meant to break up the spatial interconnection by partially spheroidizing the eutectic microstructure.

SEM backscattered electron (BSE) micrographs were obtained from the polished cross section of the ternary alloy specimens and used to determine the (area) fraction of the eutectic using the ImageJ[13] software. The micrographs were color inverted and the threshold/contrast adjusted to better differentiate the eutectic regions from the matrix. A minimum of five images were used to calculate the average area fraction of eutectic for each alloy.

Tensile testing of the ternary alloys and all of the flash-annealed specimens were carried out on a hard beam testing machine, with an extensometer attached. Four repeats were performed for each alloy and condition (as-cast and flash-annealed). The tensile data for the as-cast binary alloy specimens were reported originally in Reference 7.

D. *Finite Element Modeling*

Meshing of the 3D eutectic network was done using four-node tetrahedral elements (C3D4) through the commercial Amira 5.3™ package's built-in tools. The deformation behavior was subsequently assessed using the software package ABAQUS 6.10™.

Prior TEM examination[7] of the two binary alloys showed a very fine lamellar eutectic morphology which makes the identification of the intermetallic difficult in the SEM images of the FIB sectioning. The 3D images used in this work thus encompass the entire percolating eutectics instead of just the intermetallic. This is in contrast with the alloy AZ91D of Reference 9, for which

Table II. Parameters of the FIB Tomography

FIB Tomography			Sectioned Slices		
Source	Voltage	Current	Resolution	Slice Thickness	No. of Slices
Ga^+ ions	30 kV	1.0 nA	1024 × 884	0.2 μm	100

Further details can be found in Ref. [8].

the divorced eutectic makes the identification of the intermetallic alone more feasible, and therefore, the strengthening effects can be traced down to the percolating eutectic intermetallic. In the present case, and similarly to the prior work on Mg-Ce,[10] the reinforcing can only be traced down to the eutectic, (α-Mg)-$Mg_{12}La$ and (α-Mg)-Mg_3Nd composites.

The FEM modeling deals with the elastic behavior of the 3D eutectic structure in isolation from the pro-eutectic α-Mg matrix in which it is embedded. This is not a mere simplifying assumption: the model aims at estimating the contribution to the alloy's strength stemming from the spatial interconnection alone, and for which the interaction with the matrix is not relevant. Doing so also allows comparing the behavior of the interconnected eutectic with standard cellular structures, and so anticipates the propensity to develop damage by cracking of the intermetallic micro-trusses during deformation. The strengthening effects stemming from the interaction of the eutectic with the Mg matrix are subsequently incorporated through standard analytical expressions (*cf.* Section IV–C).

E. *Damage by Cracking of the Intermetallic*

For the purposes of the modeling, it was assumed that brittle fracture of the interconnected branches of eutectic $Mg_{12}La$ and Mg_3Nd occurred at a (local) tensile strain of 0.7 pct, in keeping with available data regarding the tensile fracture of directionally *in situ* solidified eutectics[14,15] which fail at tensile strains of 1 pct at best. A more detailed justification of the value assumed for the fracture strain (0.7 pct) was included in the authors' prior modeling work.[9,10] It was also assumed that plastic relaxation of pileup stresses on the Mg alloy matrix started at the same strain of 0.7 pct.[9] Doing so imposed a lower bound for the (local) strain to the onset of damage on the interconnected branches orientated to take a load greater than average. This strain imposed a limit to the stress taken up by the α-Mg matrix.

As for the prior FEM modeling,[9,10] the numeric simulations were limited to a maximum uniform strain of 1 pct given that the space filling α-Mg matrix was ignored in the modeling, an assumption at best valid for small strains. By the same token, the estimates of damage effects on the strength apply to very low average plastic strains, that is, they only aimed at predicting the onset of damage by cracking.

III. RESULTS

A. *3D Microstructural Features*

Figures 1(a) and 2(a) show the volumes sampled by FIB. The lighter (green) and darker (blue) areas represent, respectively, the α-Mg and the eutectic phases. The relevant microstructural information is given in Table III. The eutectics, respectively shown in Figures 1(b) and 2(b), form a profusely interconnected 3D network, closely reproducing the observations made in earlier work on AZ91D[8,9] and Mg-Ce alloys.[10] The difference in volume fraction of eutectic between the two present alloys is manifest.

B. *The (α-Mg)-Eutectic Intermetallic Composites*

The moduli, E_e, of the eutectics Mg-$Mg_{12}La$ and Mg-Mg_3Nd were determined using the rule of mixtures, assuming that the intermetallic reinforces the whole eutectic as long fibers do in a metal matrix composite[17]:

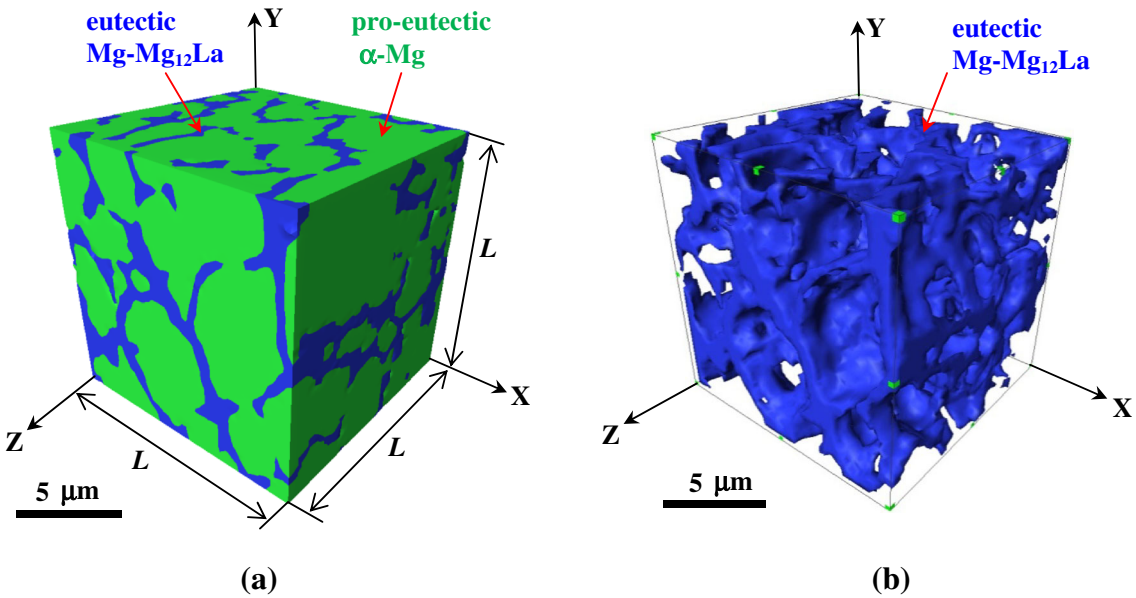

Fig. 1—(*a*) Cubic volume of the HPDC Mg-La alloy examined using FIB. The lighter phase is the pro-eutectic α-Mg, whereas the darker one is the percolating 3D (α-Mg)-$Mg_{12}La$ eutectic (3De). The latter is shown on its own in (*b*) (Color figure online).

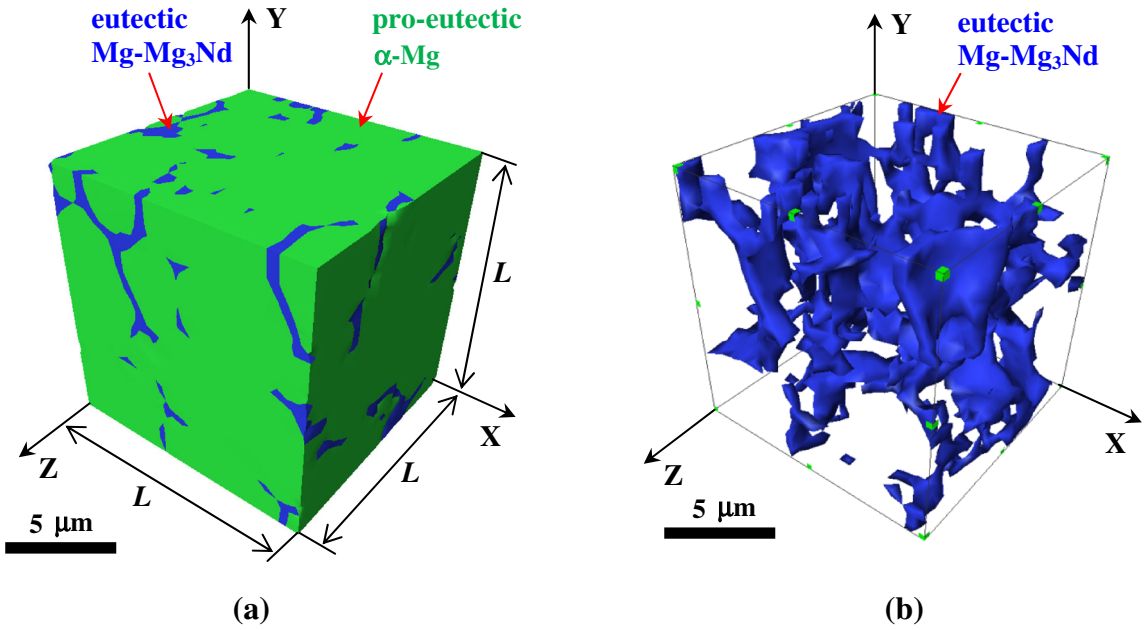

Fig. 2—(*a*) Cubic volume of the HPDC Mg-Nd alloy examined using FIB (skin region). The lighter phase is the pro-eutectic α-Mg whereas the darker one is the percolating (α-Mg)-Mg_3Nd eutectic. The latter is shown on its own in (*b*) (Color figure online).

Table III. Microstructural Information Regarding the FIB Sampled Volumes of Figs. 1(a) and 2(a): Length, *L*, of the Cube Side; Volume Fraction of the Percolating Eutectic, f^e; and the Volumetric Proportions of α-Mg, f^α; and of the Intermetallic, f^i; Within the Eutectic (α-Mg)-$Mg_{12}La$ and (α-Mg)-Mg_3Nd

Alloy	L (μm)	f^e (pct)*	f^α (pct)**	f^i (pct)**	$f^e \times f^i$ (pct)
Mg-0.62 at. pctLa	11.6	29.9	55.8	44.2	13.21
Mg-0.60 at. pctNd	11.4	7.5	69.9	30.1	2.25

The product $f^e \times f^i$ (pct) is the volumetric fraction of intermetallic phase within the sampled volumes.
*Determined using the built-in tools of the Amira software.[16]
**Determined as per the binary phase diagram.

$$E_e = f^i E_i + f^\alpha E_\alpha, \quad [1]$$

where E_i and E_α represent the respective moduli of the intermetallic and that of the eutectic α-Mg. The relevant numerical values are listed in Table IV.

In Figure 3 the elastic/plastic response of the eutectics is schematized assuming they deform as long-fiber metal matrix composites do,[17] *i.e.*, with a linear stage in which both matrix and reinforcement are elastic, followed by a stage in which plastic deformation develops in the matrix, while the fibers either remain elastic or break. The slopes, E_i, E_α, and E_e, represent the purely elastic stage for both matrix and reinforcement (the actual E values and volume fractions from Tables III and IV were used for the plot). At or past the strain of 0.7 pct (indicated by primed symbols) cracking of the intermetallic implies $E_i' = 0$, whereas plastic deformation of the matrix involves a "plastic modulus" $E_\alpha' = 1.4$ GPa.[18] Although the $Mg_{12}La$ intermetallic is somewhat more compliant than the Mg_3Nd (E_i values in Table IV), the Mg-La eutectic composite is stiffer (E_e values) due to the higher volumetric fraction of intermetallic phase (f^i values in Table III) within the eutectic. The Poisson's ratio for the eutectics was taken as 0.28 (Mg-La) and 0.3 (Mg-Nd), calculated as the average between those of pure Mg and the respective intermetallics.*

*Similar modeling[9] for alloy AZ91D showed that varying the Poisson's ratio within the range bounded by the values for the pure Mg and that of the intermetallic has negligible effects on the calculated stress–strain behavior of the percolating structure.

C. *FE Modeling*

The 3D eutectic structures of Figures 1(b) and 2(b), (referred from here on as 3De), were bounded by two rigid shells as shown in Figure 4. A force, F, applied perpendicularly to the top shell results in a displacement, δ, parallel to the Y-axis. The average stress, σ_{3De}, and strain, ε, experienced by the 3De, and its effective elastic modulus, E_{3De}, are given by:

$$\varepsilon = \ln(1 + \delta/L), \quad [2]$$

$$\sigma_{3De} = (1 + \delta/L) * F/L^2, \quad [3]$$

Table IV. Elastic Moduli, E_i, for the $Mg_{12}La$ and Mg_3Nd Intermetallics, α-Mg, E_α, and Eutectic (α-Mg)-$Mg_{12}La$ and (α-Mg)-Mg_3Nd Composites, E_e

Alloy	E_i (GPa)	E_i' (GPa)	E_α (GPa)	E_α' (GPa)	E_e (GPa)	E_e' (GPa)
Mg-0.62 at. pctLa	66.9[19]	0	44[20]	1.4[18]	54.1	0.78
Mg-0.60 at. pctNd	70.3[21]				51.9	0.98

Primed values indicate the behavior after either cracking of the intermetallic (E_i') and/or the onset of plastic deformation of the α-Mg, (E_α', E_e') within the eutectic past the strain of 0.007 (Fig. 3).

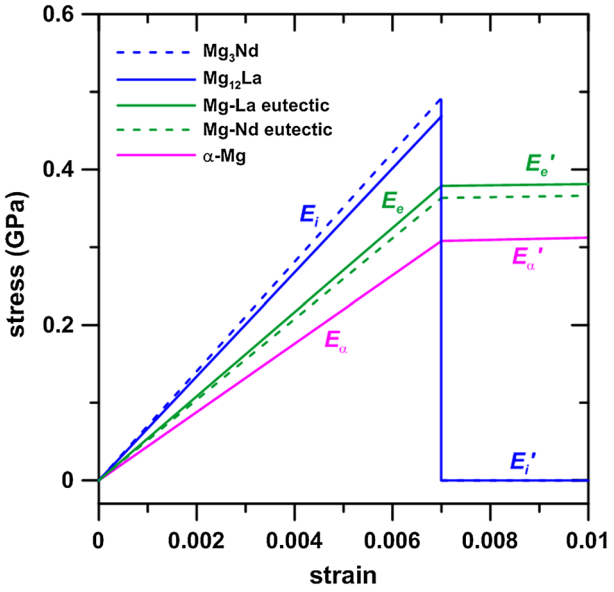

Fig. 3—Schematic representation of the elastic (E_i, E_e, E_α), plastic (E_α'), or post-fracture (E_e', E_i') response of the intermetallic phase, the α-Mg matrix and the eutectic composites. The E values are the slopes of the respective lines as per the numerical values of Tables III and IV).

$$E_{3De} = \sigma_{3De}/\varepsilon. \quad [4]$$

Four-node tetrahedral elements (C3D4)[22] were used to discretize the eutectic networks. Convergence of results was obtained with ~110,000 and ~28,000 C3D4 elements, respectively, for the Mg-$Mg_{12}La$ and Mg-Mg_3Nd networks.

In Figure 5 the solid lines, with slope E_{3De}, represent the elastic deformation of the two 3D networks. The Mg-La network appears stiffer by one order of magnitude than the Mg-Nd one (note that the left hand Y-axis corresponds to the Mg-La alloy only). The dashed lines show that the cumulative effect of cracking of the intermetallic micro-trusses and plastic deformation of the matrix, both assumed to occur at a (local) strain of 0.7 pct as per Figure 3. The deviations from linearity at ~0.3 pct strain indicate that some micro-trusses are already overloaded in both 3D networks at very low (average) stresses and strains.

The distributions of local strains are shown in Figures 6 and 7 for applied (uniform) tensile strains of 0.4 and 1 pct. The black regions indicate where plastic relaxation of the matrix and cracking of the interconnecting branches are expected to occur. The Mg-La network (Figure 6) exhibits a greater tendency to crack, consistently with its earlier departure from linearity in Figure 5 and the concomitant drop in strength.

D. *Ternary Alloys, Flash-Anneals*

The volume fractions of the eutectic, f^e, in as-cast ternary alloys are listed in Table V.

Figures 8(a) through (c) show that the flash-annealing led to marked globularization of the eutectic, indicating a breaking up of the percolating network in all of the alloys. Flash-annealing was not applied to Mg-0.60at. pctNd since its low volume fraction (Table III) of eutectic precludes any meaningful spatial interconnection.

Figures 9(a) through (c) show the decrease in strength caused by the flash-anneals (measured on the vertical lines at ~0.06 total strain, corresponding to the (0.2 pct offset strain) yield strength), which amount to 44 and 30 MPa for the ternary alloys and 34 MPa for the binary alloy, respectively.

IV. DISCUSSION

A. *Structural Behavior*

To better characterize the behavior of the 3D networks, their elastic responses are compared in Figure 9 with those of standard hybrid model structures,[23,24] namely, fiber composites and foamed/lattice structures. This was done using standard equations for upper and lower bounds.**

**In Reference 9 the intermetallic network of alloy AZ91D was considered under a compressive stress in the undeformed alloy due to the difference in the coefficient of thermal expansion (CTE) between Mg matrix and the intermetallic. In the present case, the intermetallic and surrounding eutectic α-Mg are considered as a unit, and any internal stresses arising from thermal effects between the two components were assumed to balance out.

The Reuss and Voigt bounds, labeled E_{RB} and E_{VB}, represent, respectively, the lower and upper limits to the elastic modulus of long-fiber composites[23]:

$$E_{RB} = \frac{E_m E_e}{f^e E_m + (1 - f^e) E_e} \quad \text{(Reuss' bound)}, \quad [5]$$

$$E_{VB} = f^e E_e + (1 - f^e) E_m \quad \text{(Voigt's bound)}, \quad [6]$$

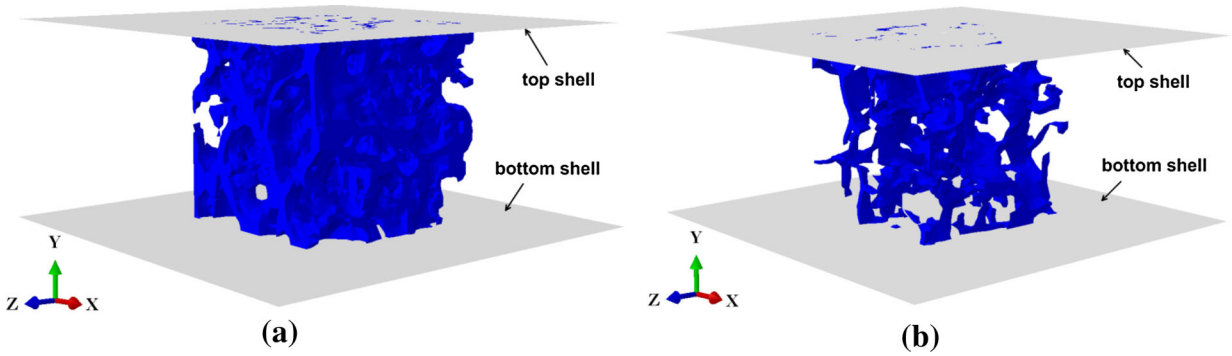

Fig. 4—FE model setup for loading of the interconnected eutectics. The loading was applied in the *Y*-direction: (*a*) Mg-$Mg_{12}La$ eutectic; (*b*) Mg-Mg_3Nd eutectic.

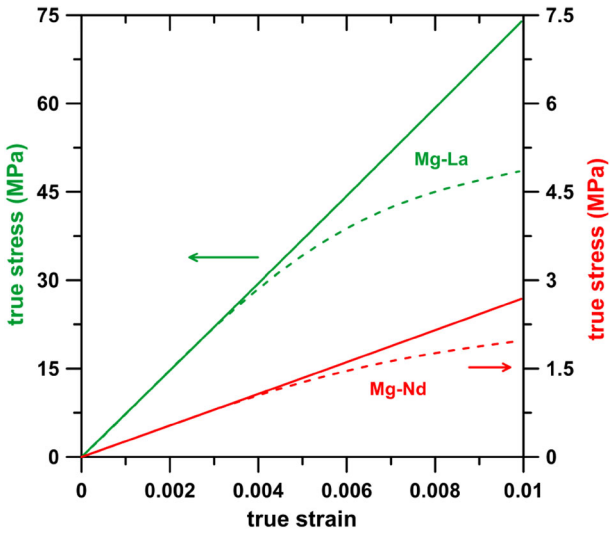

Fig. 5—The solid lines are the calculated linear-elastic response of the eutectic networks (E_{3De}, Eq. [4]); the dashed lines represent the behavior assuming that cracking of the intermetallic and plastic deformation of the α-Mg matrix occur at local strains of 0.7 pct and above.

where E_m (=0) represents the open spaces in Figures 1(b) and 2(b).

The upper and lower bounds of foamed solids, E_{BD} and E_{SD}, for bending-dominated and stretch-dominated structures,[†] respectively, were calculated as:

[†]In comparison with the Voigt's bound, which assumes all micro-trusses aligned parallel to the stress axis, in the SD configuration only 1/3 of the interconnected branches are loaded in tension, with the rest orientated across the tensile axis. In the BD configuration loads are transmitted exclusively through elastic bending of the micro-trusses.[24]

$$E_{BD} = (f^e)^2 E_e, \quad [7]$$

$$E_{SD} = \frac{f^e E_e}{3}. \quad [8]$$

Figure 9 shows that the Mg-$Mg_{12}La$ network is slightly stiffer than the stretch-dominated model structure, whereas the Mg-Mg_3Nd closely matches the behavior of a bending-dominated structure. Note that the volume fraction of the present Mg-Mg_3Nd network (7.5 pct, in Table III) is similar to that of the $Mg_{17}Al_{12}$ network in AZ91D alloy (5 to 13 pct) which also exhibits bending-dominated behavior.[9]

B. *Structural Efficiency and Damage Generation*

A hard phase dispersed in a metallic matrix, including long-fiber reinforced composites, is expected to increase both the elastic modulus and the strain hardening rate in comparison with those of the unreinforced alloy, in proportion to the volume fraction *times* the elastic modulus of the reinforcement.[25–28] Damage by cracking of the reinforcement decreases the intensity of the reinforcing, lowering first the elastic slope and later the strain hardening rate of the composite.[29–32] In a structurally efficient stretch-dominated structure, (*e.g.*, unidirectional fiber composites), the reinforcing effect is, by necessity, constrained to low strains due to early fracture of the reinforcement. The highly compliant, low-efficiency bending-dominated structures, sacrifice the initial stiffening in favor of a delayed onset of damage by cracking, and can, therefore, be expected to extend the overall reinforcement well into the plastic regime of the matrix. Being closer to the stretch-dominated behavior in Figure 9, the Mg-$Mg_{12}La$ network is expected to introduce a much larger strengthening at low strains, but at the same time a greater tendency to crack locally, already made evident in Figures 5 and 6. Conversely, the Mg-Mg_3Nd network is expected to introduce a more limited strengthening, but also delayed cracking, consistent with bending-dominated behavior. In more practical terms, cracking by stretching of the interconnected branches is expected to impose a lower limit to the ductility in the Mg-La alloy. A more detailed discussion on the effect of delayed cracking of the interconnected intermetallic when it behaves like a bending-dominated structure can be found in Reference 9 with reference to HPDC alloy AZ91. (Ductility effects are discussed in further detail with reference to Figure 14.)

It should be noticed that whether a 3D network behaves as either stretch-dominated or bending-

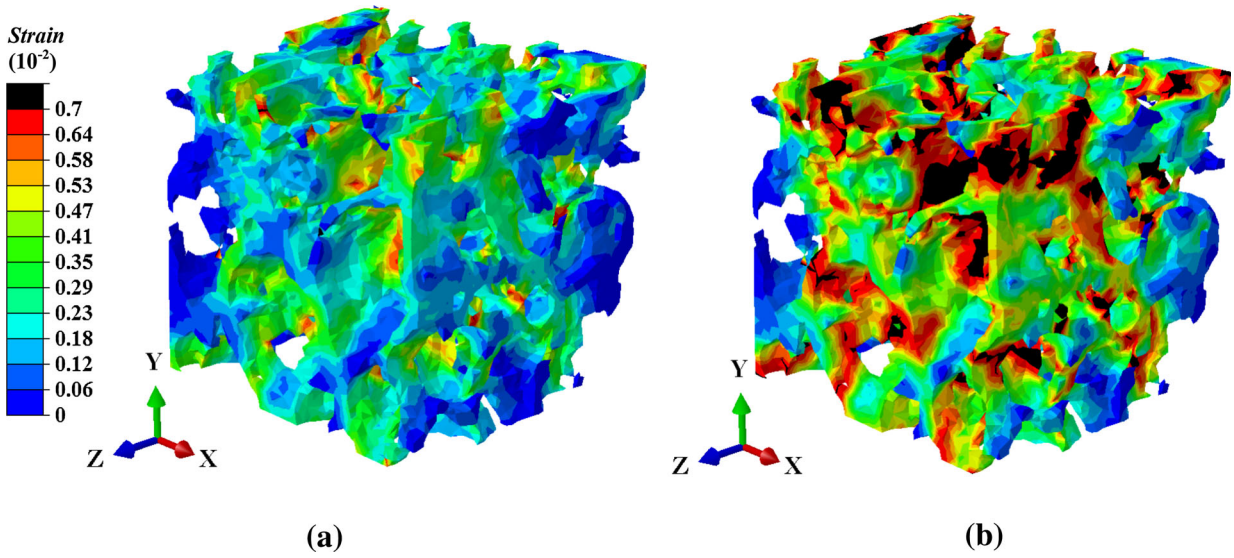

Fig. 6—Distributions of local strains in the Mg-$Mg_{12}La$ network stretched in tension by (*a*) 0.4 pct and (*b*) 1 pct strain. The black regions identify cracking of the intermetallic (Color figure online).

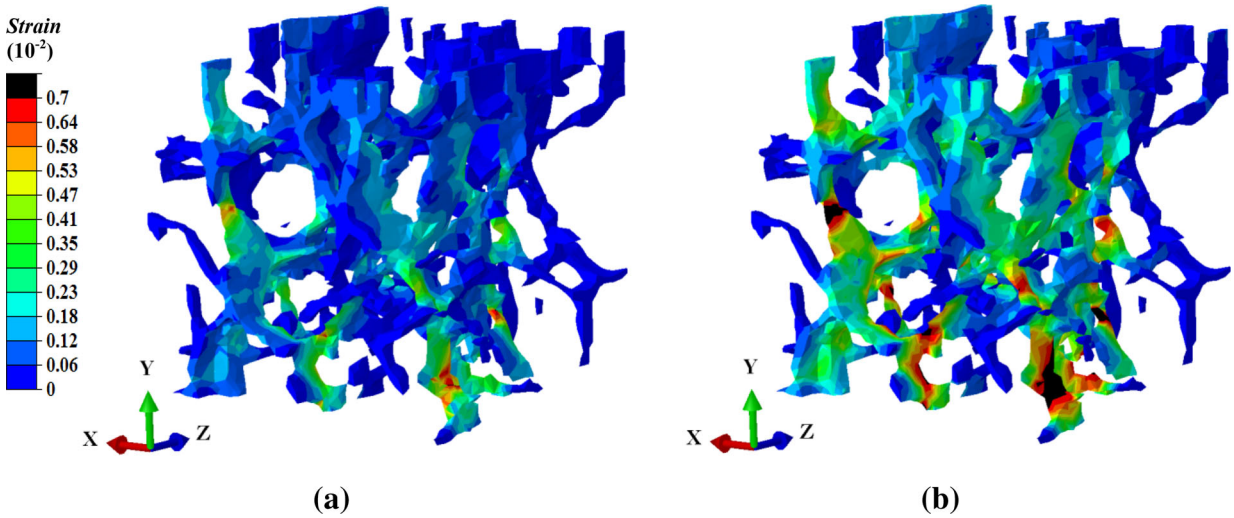

Fig. 7—Distributions of local strains in the Mg-Mg_3Nd network stretched in tension by (*a*) 0.4 pct and (*b*) 1 pct strain. The black regions identify cracking of the intermetallic.

dominated is solely a function of the degree of interconnection. This has important practical consequences for the present alloys: the degree of interconnection, that is, the tendency to exhibit stretch-dominated behavior, for comparable grain size and solute content, is expected to increase with the volume fraction of eutectic, which, in turn, increases when the solute has low solid solubility. Such is the case of the Mg-La alloy in Figure 9.

C. *Strengthening Effects*

The drop in strength due to the flash-anneal shown by Figure 10, in conjunction with the microstructural changes (Figure 8), provides strong support to the hypothesis that the spatial interconnection contributes a significant amount to the total strength of the alloys. The modeling provides further supporting evidence for the binary alloys, as detailed next.

The strength of the as-cast specimens, $\sigma_{\text{as-cast}}$ can be approximated by adding the calculated network strength (σ_{3De}, Figure 5), to the strength of the relevant flash-annealed, $\sigma_{F\text{-}a}$, specimens of Figure 10(c), *i.e.*,

$$\sigma_{as-cast} = \sigma_{F-a} + \sigma_{3De}. \quad [9]$$

Comparison with the experimental data for the Mg-0.62at. pctLa binary alloy is shown in Figure 11, with the most remarkable agreement.

Alternatively, the strength of the as-cast Mg-0.62at. pctLa can be estimated with reference to a dilute (eutectic-free) Mg-0.09at. pctLa alloy, replotted from Reference 7) in Figure 12, considering that adding a 3D eutectic phase should introduce dispersion hardening, σ_{disp}, in addition to the spatial interconnection, σ_{3De}, effects. The former is easily quantified using standard equations.[25–27]

Table V. Volume Fraction of Eutectic, f^e, in the (As-Cast) Ternary Alloy, Compared with Those of the Binary Alloys in Table III

Ternary Alloys	f^e (pct)*	Binary Alloys	f^e (pct)**
Mg-0.47 at. pctLa-0.10 at. pctNd	16.7	Mg-0.60 at. pctNd	7.5
Mg-0.45 at. pctLa-0.63 at. pctNd	24.7	Mg-0.62 at. pctLa	29.9

*Measured as area fraction on SEM images *via* ImageJ software.[13]
**Determined using the built-in tools of the Amira software.[16]

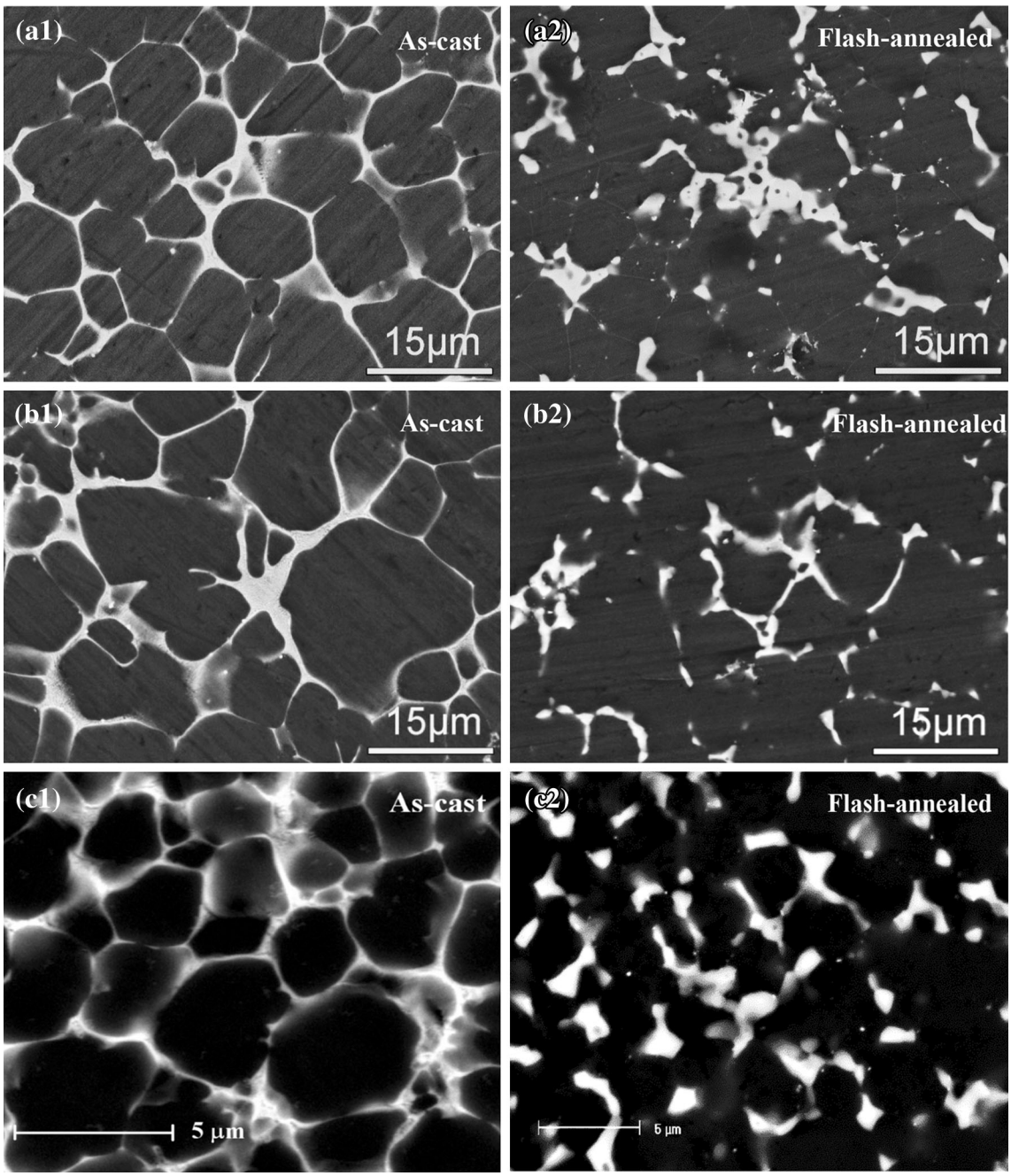

Fig. 8—SEM BSE micrographs (*a1*) as-cast Mg-0.45La-0.63Nd, (*a2*) flash-annealed Mg-0.45La-0.63Nd, (*b1*) as-cast Mg-0.47La-0.10Nd, (*b2*) flash-annealed Mg-0.47La-0.10Nd, (*c1*) as-cast Mg-0.62La, (*c2*) flash-annealed Mg-0.62La alloys.

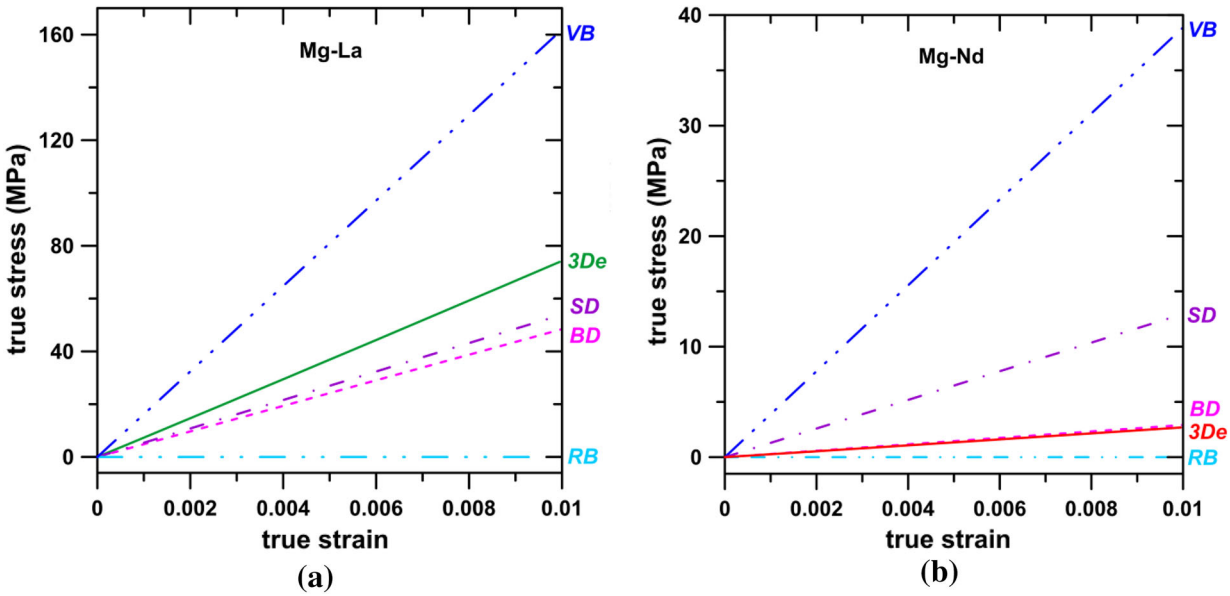

Fig. 9—Stress–strain responses of the eutectic networks (3De), compared with those of model structures as per Eqs. [5] through [8], namely: Voigt bound (VB); stretch-dominated behavior (SD); bending-dominated behavior (BD); Reuss bound (RB). (*a*) Mg-$Mg_{12}La$; (*b*) Mg-Mg_3Nd.

$$\frac{d\sigma_{disp}}{d\varepsilon_p} = E_i f^e f^i \quad (<0.7\,\text{pct}), \qquad [10a]$$

$$\frac{d\sigma_{disp}}{d\varepsilon_p} = 1.4\,\text{GPa} \quad (>0.7\,\text{pct}), \qquad [10b]$$

where ε_p denotes true plastic strain.[‡]

[‡]For $\varepsilon < 0.7$ pct, the strain hardening rate reflects the rapid development of a back stress due to the formation of dislocation pile ups on the obstacles to primary micro-slip, whereas for $\varepsilon > 0.7$ pct, linear hardening is observed due to the steady accumulation of forest dislocations when full plasticity develops.[17,25,33]

Again, assuming linear addition, the as-cast specimen's strength becomes:

$$\sigma_{as-cast} = \sigma_{dil} + \sigma_{disp} + \sigma_{3De}, \qquad [11]$$

where σ_{dil} represents the strength of the (eutectic-free) as-cast dilute alloy in Figure 12. Again, as for Figure 11, the calculated strength closely agrees with the experimental data.

A similar validation of the present numerical approach stems from Figures 10(a) and (b), which show that the breakup of the spatial interconnection leads to a drop in the (0.2 pct offset) yield strength of 44 and 30 MPa, respectively, for the ternary alloys. These two values for the loss of strength, once again, are in very close agreement with the estimated network strengthening (Figure 12) of 37 MPa for the Mg-La alloy.

The procedure leading to Figure 12 is repeated for the as-cast binary Mg-0.60at. pctNd alloy in Figure 13, using the flow curve of the (eutectic-free) Mg-0.08at. pctNd alloy from Reference 7 as a reference. In this case, a shortfall of 35 MPa in the calculated yield strength is seen.

The difference between the two alloy systems can be rationalized considering that La exhibits no solid solubility in Mg[7], whereas Nd is fairly soluble[33] and thus a significant solid solution strengthening is expected for the latter. There seems to be no data on the strength of Nd-related solid solution hardening. However, the published data on Mg-Zn, Mg-Gd, and Mg-Y alloys[34–36] suggest that at solute concentrations of 0.4 and 1.5 at. pct, solid solution strengthening and short range order (SRO)[36–38] combine to add ~15 and ~70 MPa, respectively, to the yield strength of the alloy. Assuming similar strengthening effects for Nd, 0.60 at. pctNd in solution should add ~30 MPa to the alloy strength, thus accounting for the shortfall in Figure 13. The 3D Mg-Nd network contributes a negligible 1.4 MPa at yield (Figure 13), consistently with the very limited amount of Mg-Nd intermetallic and eutectic phases (Table III).

An overview of the alloys behavior is presented in Figure 14, in both as-cast and flash-annealed conditions. Aside from the expected increase in ductility, the annealed specimens exhibited a lower slope in the microplasticity region prior to the development of general plasticity (made evident already in Figure 10). Both effects—increased ductility and lower apparent stiffness at low strains—are consistent with the behavior expected from the breaking up of the 3D network in the flash-annealed specimens, as mentioned with regards to Figure 5.[§]

[§]The increase in ductility of the flash-annealed specimens is not as large as it might be expected from Fig. 5. Possible factors to invoke are the cracking of the intermetallic overloaded by dispersion hardening effects, and the presence of microporosity, which can have an overriding effect on the tensile ductility.

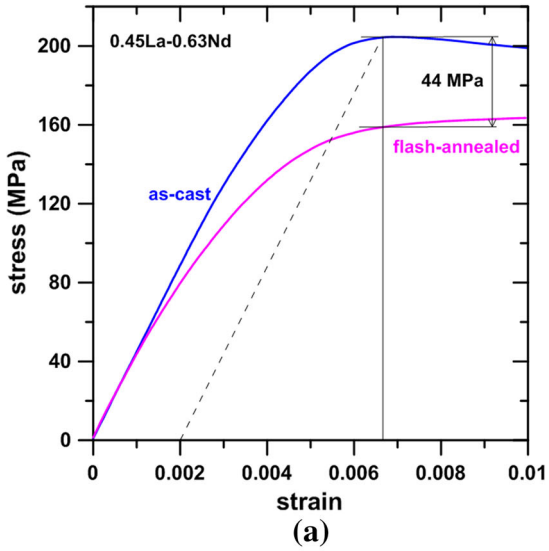

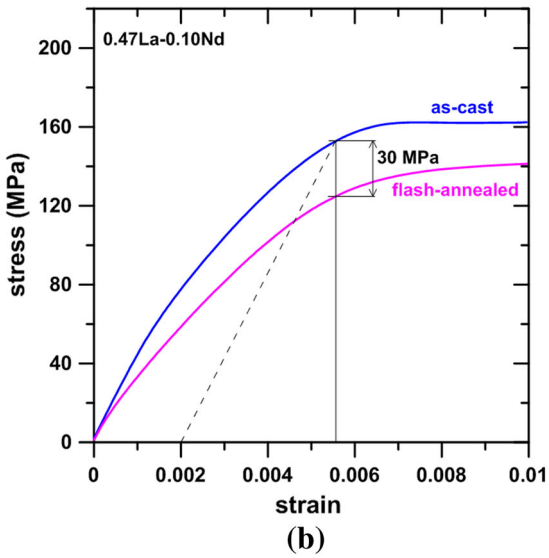

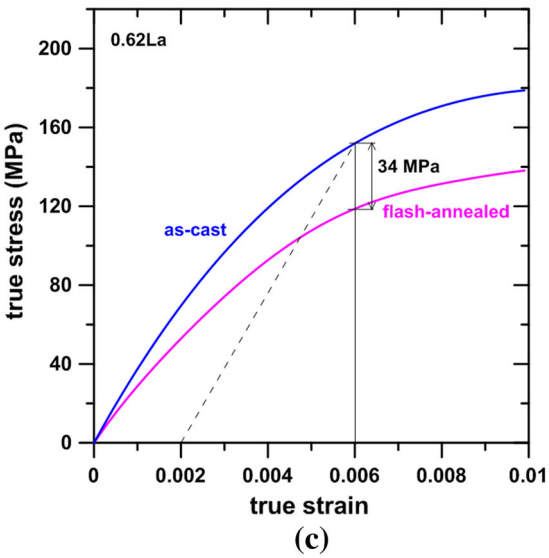

◀Fig. 10—Stress–strain curves of as-cast and flash-annealed tensile specimens of (*a*) Mg-0.45at. pctLa-0.63at. pctNd, (*b*) Mg-0.47at. pctLa-0.10at. pctNd, (*c*) Mg-0.62at. pctLa. The slope of the dashed lines matches the elastic modulus of Mg (44 GPa[20]). The curve labeled "as-cast" in (c) was replotted from Ref. [7].

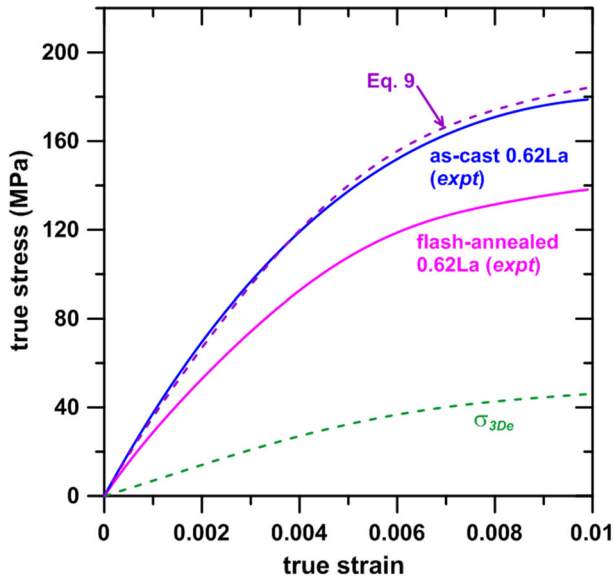

Fig. 11—The network contribution to the alloy strength, σ_{3De} (the dashed line of Fig 5), the linear addition (as per Eq. [9]) of the flash-annealed 0.62La alloy, and the σ_{3De} line, compared with the experimental flow curve of the as-cast Mg-0.62at. pctLa specimen (the solid lines as in Fig. 10(c)).

Figures 12 through 14 suggest that an optimal combination of strengthening mechanisms should involve a high volume fraction of a thermally stable percolating eutectic network, *e.g.*, through a high content of La, and a strong residual solid solution hardening (SRO), *e.g.*, through Nd. This optimal situation is closely represented by the Mg-0.45La-0.63Nd alloy of Figure 10(a).

To close the discussion, two aspects of the modeling deserve some qualification: (i) the interaction between matrix and intermetallic was ignored; (ii) the FIB data were collected over a rather minute scale (~20 μm) at one specific location (near the corner of tensile bars), but then used to represent the whole cross section of the castings, which is known to involve gradients of grain size, eutectic content, and degree of interconnection.[2,39–41] (An example of detailed modeling of the different strengthening mechanism operations of HPDC alloys explicitly accounting for microstructural gradients can be found elsewhere.[42])

For the first point, the relatively low strains considered ensured that the assumption remained realistic, whereas the main effects of the interaction between the eutectic and Mg matrix are accounted for by the calculated dispersion hardening (Eq. [10]). For the second, it must be kept in mind that the strength of

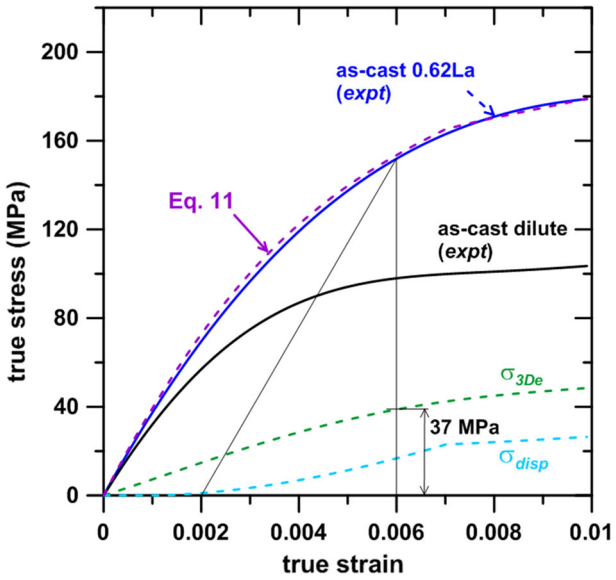

Fig. 12—The calculated strength (σ_{disp}, Eq. [10], and σ_{3De}, dashed line in Fig. 5), the experimental flow curve of a Mg-0.09at. pctLa alloy (as-cast dilute, replotted from Ref. [7]), and their linear addition, $\sigma_{as\text{-}cast}$ (Eq. [11]), compared with the experimental flow curve of the as-cast Mg-0.62at. pctLa (Fig. 10(c)) alloy. (*Note* with regards to σ_{disp} that the *x*-axis in this figure is the total (elastic + plastic) strain whereas Eq. [10] is a (*linear*) function of the plastic strain only.)

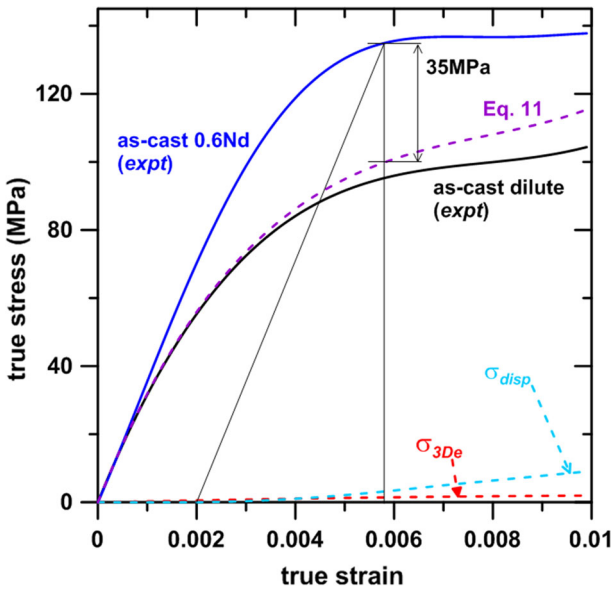

Fig. 13—The calculated strength (σ_{disp}, Eq. [10], and σ_{3De}, Fig. 5), the experimental stress–strain curve of a Mg-0.08at. pctNd alloy (as-cast dilute), and their linear addition, $\sigma_{as\text{-}cast}$ (Eq. [11]), compared with the experimental flow curve of the as-cast Mg-0.60at. pctNd alloy. Experimental curves are replotted from Ref. [7]

HPDC alloys stems from the skin region.[2,43] Being stronger, the skin applies a elastic constraint on the weaker parts of the cross section (the core), and this makes the skin's strength the determining factor on the deformation behavior of the entire casting. Thus, FIB-sampling the microstructure at the point where it is

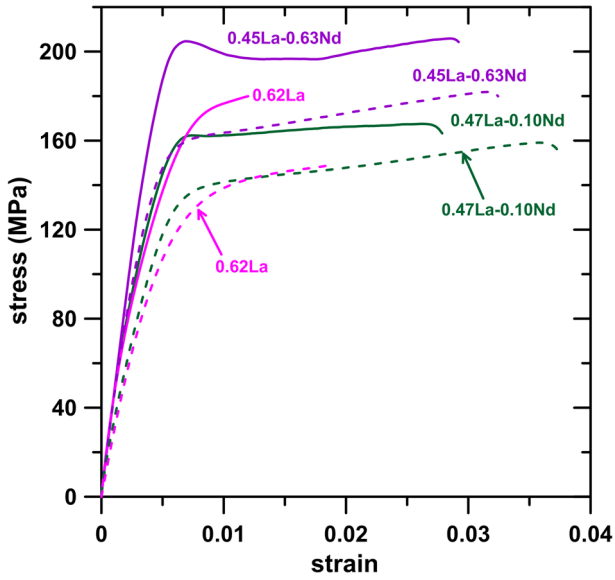

Fig. 14—Stress–strain behavior of the binary and ternary alloys up to fracture. The solid and dashed lines correspond, respectively, to as-cast and flash-annealed conditions; the small strain behavior (<1 pct strain) can be seen in more detail in Fig. 10.

finest in grain size and strongest, *i.e.*, at the corner of the cross section, seems to be the logical approach. Given the relative simplicity of the present approach, the excellent agreement between calculated and predicted values is certainly encouraging.

V. CONCLUSIONS

1. 3D FIB tomography revealed a closely spatially interconnected network of eutectic (α-Mg)-$Mg_{12}La$ and (α-Mg)-Mg_3Nd, respectively, in HPDC Mg-0.62at. pctLa and Mg-0.60at. pctNd alloys.
2. FEM modeling indicated a high compliance of the (α-Mg)-Mg_3Nd network, akin to that of a bending-dominated cellular or micro-truss lattice-structure, and a much higher stiffness for the (α-Mg)-$Mg_{12}La$ network, close to that of a stretch-dominated structure. The tendency of any alloy to exhibit stretch-dominated behavior increases with the volume fraction of eutectic, reflecting the increased spatial interconnection.
3. The high compliance of Mg-Nd 3D network implies a low rate of cracking of the eutectic branches in comparison with the Mg-La network, for which damage by cracking was predicted to develop rapidly from low strains with an overall reduced ductility. This prediction was generally matched by the experiments.
4. The modeling combined with experimental flow curves for dilute (eutectic-free) alloys indicates that the Mg-La 3D eutectic network should contribute ~37 MPa to the strength of the alloy against 1.4 MPa by the Mg-Nd network.
5. Break up of the 3D network in the binary Mg-La and the ternary Mg-La-Nd alloys through flash-anneals led to reductions in the alloys' strengths of 30

to 44 MPa, closely matching the model's prediction (~37 MPa).

REFERENCES

1. C.H. Cáceres, W.J. Poole, A.L. Bowles, and C.J. Davidson: *Mater. Sci. Eng. A*, 2005, vol. 402, pp. 269–77. DOI:10.1016/j.msea.2005.04.024.
2. K.V. Yang, C.H. Caceres, A.V. Nagasekhar, and M.A. Easton: *Mater. Sci. Eng. A*, 2012, vol. 542, pp. 49–55. DOI:10.1016/j.msea.2012.02.029.
3. D. Amberger, P. Eisenlohr, and M. Goken: *Acta Mater.*, 2012, vol. 60, pp. 2277–89. DOI:10.1016/j.actamat.2012.01.017.
4. B.S. Shin, J.W. Kwon, and D.H. Bae: *Met. Mater. Int.*, 2009, vol. 15, pp. 203–207. DOI:10.1007/s12540-009-0203-8.
5. T. Aune and H. Westengen, ed.: *SAE Technical Paper 950424*, SAE, Warrendale, PA, 1995), pp. 332–42.
6. D.J. Sakkinen, ed.: in *SAE Technical Paper 940779*, SAE, Warrendale, PA, 1994, pp. 558–69.
7. T.L. Chia, M.A. Easton, S.M. Zhu, M.A. Gibson, N. Birbilis, and J.F. Nie: *Intermetallics*, 2009, vol. 17, pp. 481–90. DOI:10.1016/j.intermet.2008.12.009.
8. A.V. Nagasekhar, C.H. Caceres, and C. Kong: *Mater. Charact.*, 2010, vol. 61, pp. 1035–42. DOI:10.1016/j.matchar.2010.06.007.
9. B. Zhang, A.V. Nagasekhar, T. Sivarupan, and C.H. Caceres: *Adv. Eng. Mater.*, 2013, vol. 15, pp. 1059–67. DOI:10.1002/adem.201300138.
10. B. Zhang, A.V. Nagasekhar, X. Tao, Y. Ouyang, C.H. Caceres, and M. Easton: *Mater. Sci. Eng. A*, 2014, vol. 599, pp. 204–211. DOI:10.1016/j.msea.2014.01.074.
11. S. Gavras, S.M. Zhu, M.A. Gibson, M.A. Easton, and J.F. Nie: in *Magnesium 2012: 9th International Conference on Magnesium Alloys and Their Applications*, W.J. Poole and K.U. Kainer, eds., Vancouver, 2012, pp. 757–62.
12. M.A. Easton, M.A. Gibson, D. Qiu, S.M. Zhu, J. Grobner, R. Schmid-Fetzer, J.F. Nie, and M.X. Zhang: *Acta Mater.*, 2012, vol. 60, pp. 4420–30. DOI:10.1016/j.actamat.2012.04.039.
13. ImageJ: *Image Processing and Analysis in Java*. http://rsb.info.nih.gov/ij/, Accessed 24 Oct 2013.
14. B. Cantor and G.A. Chadwick: *J. Mater. Sci.*, 1975, vol. 10, pp. 578–88. DOI:10.1007/BF00566564.
15. M. Sahoo and R.W. Smith: *Met. Sci.*, 1975, vol. 9, pp. 217–22. DOI:10.1179/030634575790444874.
16. Amira: *Amira 3.1 User's Guide and Reference Manual*. http://www.amira.com/documentation.html, Accessed 5 Sept 2011.
17. D. Hull: *An Introduction to Composite Materials*, Cambridge University Press, Cambridge, 1981.
18. C.H. Cáceres and P. Lukác: *Philos. Mag. A*, 2008, vol. 88, pp. 977–89. DOI:10.1080/14786430801968611.
19. J. Wrobel, L.G. Hector, Jr, W. Wolf, S.L. Shang, Z.K. Liu, and K.J. Kurzydlowski: *J. Alloys Compd.*, 2012, vol. 512, pp. 296–310. DOI:10.1016/j.jallcom.2011.09.085.
20. T. Sumitomo, C.H. Cáceres, and M. Veidt: *J. Light Met.*, 2002, vol. 2, pp. 49–56. DOI:10.1016/S1471-5317(02)00013-5.
21. H. Zhang and S. Wang: *Acta Metall. Sin.*, 2012, vol. 48, pp. 889–94. DOI:10.3724/SP.J.1037.2012.00089.
22. O.C. Zienkiewicz and R.L. Taylor: *The Finite Element Method*, McGraw-Hill, Maidenhead, 1989.
23. M.F. Ashby and Y.J.M. Brechet: *Acta Mater.*, 2003, vol. 51, pp. 5801–21. DOI:10.1016/S1359-6454(03)00441-5.
24. V.S. Deshpande, M.F. Ashby, and N.A. Fleck: *Acta Mater.*, 2001, vol. 49, pp. 1035–40. DOI:10.1016/S1359-6454(00)00379-7.
25. L.M. Brown and W.M. Stobbs: *Philos. Mag.*, 1971, vol. 23, pp. 1185–99. DOI:10.1080/14786437108217405.
26. L.M. Brown and W.M. Stobbs: *Philos. Mag.*, 1971, vol. 23, pp. 1201–33. DOI:10.1080/14786437108217406.
27. M.A. Gharghouri, G.C. Weatherly, J.D. Embury, and J. Root: *Philos. Mag. A*, 1999, vol. 79, pp. 1671–96. DOI:10.1080/01418619908210386.
28. C.H. Cáceres, J.R. Griffiths, and P. Reiner: *Acta Mater.*, 1996, vol. 44, pp. 15–23. DOI:10.1016/1359-6454(95)00171-6.
29. C.H. Cáceres: *Alum. Trans.*, 1999, vol. 1, pp. 1–13.
30. Y. Brechet, J.D. Embury, S. Tao, and L. Luo: *Acta Metall. Mater.*, 1991, vol. 39, pp. 1781–86. DOI:10.1016/0956-7151(91)90146-R.
31. C.H. Cáceres and J.R. Griffiths: *Acta Mater.*, 1996, vol. 44, pp. 25–33. DOI:10.1016/1359-6454(95)00172-8.
32. P.J. Withers, W.M. Stobbs, and O.B. Pedersen: *Acta Metall.*, 1989, vol. 37, pp. 3061–84. DOI:10.1016/0001-6160(89)90341-6.
33. L.L. Rokhlin: *Magnesium Alloys Containing Rare Earth Metals*, Taylor & Francis, New York, 2003.
34. L. Gao, R.S. Chen, and E.H. Han: *J. Alloys Compd.*, 2009, vol. 472, pp. 234–40. DOI:10.1016/j.jallcom.2008.04.049.
35. L. Gao, R.S. Chen, and E.H. Han: *J. Alloys Compd.*, 2009, vol. 481, pp. 379–84. DOI:10.1016/j.jallcom.2009.02.131.
36. A.H. Blake and C.H. Cáceres: *Mater. Sci. Eng. A*, 2008, vols. 483–484, pp. 161–63. DOI:10.1016/j.msea.2006.10.205.
37. D.S. Gencheva, A.A. Katsnel'son, L.L. Rokhlin, V.M. Silonov, and F.A. Khavadzha: *Fiz. Metal. Metalloved.*, 1981, vol. 51, pp. 788–93.
38. C.H. Caceres and S. Abaspour: in *Magnesium Technology*, N. Hort, S.N. Mathaudhu, N.R. Neelameggham, and M. Alderman, eds., TMS, Wiley, 2013, pp. 225–30. DOI:10.1002/9781118663004.
39. H.I. Laukli, O. Lohne, S. Sannes, H. Gjestland, and L. Arnberg: *Int. J. Cast Met. Res.*, 2003, vol. 16, pp. 515–21.
40. H.I. Laukli, C.M. Gourlay, and A.K. Dahle: *Metall. Mater. Trans. A*, 2005, vol. 36, pp. 805–818. DOI:10.1007/s11661-005-1011-5.
41. K.V. Yang, M.A. Easton, and C.H. Caceres: *Mater. Sci. Eng. A*, 2013, vol. 580, pp. 191–95. DOI:10.1016/j.msea.2013.05.017.
42. K.V. Yang, C.H. Caceres, and M.A. Easton: *Metall. Mater. Trans. A*, 2014, in press. DOI:10.1007/s11661-014-2326-x.
43. K.V. Yang, C.H. Caceres, and M.A. Easton: *Mater. Sci. Eng. A*, 2013, vol. 580, pp. 355–61. DOI:10.1016/j.msea.2013.05.018.